Electron Spin Echo and Coherence Times in Silicon Carbide Defects

Kyle G. Miller

A senior thesis submitted to the faculty of
Brigham Young University
in partial fulfillment of the requirements for the degree of

Bachelor of Science

John Colton, Advisor

Department of Physics and Astronomy

Brigham Young University

April 2015

ABSTRACT

Electron Spin Echo and Coherence Times
in Silicon Carbide Defects

Kyle G. Miller
Department of Physics and Astronomy, BYU
Bachelor of Science

Electrons located in silicon vacancies of 4H silicon carbide (SiC) are potential spintronic devices. In our experiments, electron spin states are polarized with 870 nm laser light, and we manipulate the spins with resonant microwaves at 10.47 GHz and a magnetic field of 350 mT. Spin polarizations are detected by the change in photoluminescence from the silicon vacancy defects, and lifetimes are calculated via measurements of optically detected spin resonance and electron spin echo. We have measured T_2 lifetimes in 10^{14} cm^{-2} proton-irradiated SiC to be about 16 μs between 6 and 295 K, fairly independent of temperature. A sample with decreased defect density, proton-irradiated at 10^{13} cm^{-2}, had a lifetime of about 64 μs. A 10^{17} cm^{-2} electron-irradiated sample had a lifetime longer than we could measure. These results show that we can increase lifetime by varying defect concentration and type.

Keywords: spin echo, silicon carbide, quantum computing

ACKNOWLEDGMENTS

I would like to acknowledge Dr. John Colton for giving me continued direction and motivation, even during incredibly difficult moments in my research. I also wish to thank Dr. Ross Spencer for taking a lot of time to write efficient code for me, as well as Daniel Craft and Stephen Erickson for introducing me to this project and working with me. Finally, I wish to acknowledge funding for this project from the BYU Physics department, a BYU ORCA Grant, and from the REU program at BYU, NSF Grant PHY1157078.

Contents

List of Figures

List of Tables

Chapter 1

Introduction

1.1 Overview and Motivation

In this thesis we explore the effects of temperature, defect concentration and defect type on electron spin lifetimes in silicon carbide (SiC). Lifetimes are measured to characterize SiC for use in quantum computing as a possible spintronic device. Quantum computing involves manipulating a quantum state instead of a classical bit for calculations [1]. While a classical bit represents either a 0 or a 1, a quantum bit, or qubit, represents a superposition of states. By allowing these quantum states to interact and interfere, complicated calculations can be performed with greater efficiency. For example, the required time for a quantum computer using Shor's algorithm [2] to factor a large number N is only polynomial in $\log N$ compared to exponential in N for a classical computer [3]. Since the development of this algorithm in 1994, much work has been done to create a fully-functional quantum computer [4–8].

However, the quest for a quantum computer is difficult at best. These computers require thousands of qubits, and the quantum states must remain coherent for a sufficiently long time to perform the calculation [9]. One estimate is that each individual step in a calculation must be completed

in about one ten-thousandth of the coherence time [10]. Quantum decoherence can occur from almost any interaction with the outside world, but there are also intrinsic properties that can cause decoherence. These properties include nuclear spin interactions, lattice vibrations, and interacting with quantum gates. Such effects cannot be avoided entirely, but their impact can be minimized. A qubit system with a long coherence time will help minimize the problem of decoherence.

Many types of quantum systems exist that could be used to make a qubit, such as photons [11], electrons [12], Bose-Einstein condensates [13], and quantum dots [14]. Each has its own benefits and drawbacks. In this thesis we focus on electron spin states, which are discussed in Section 1.2.2. Various materials are currently under investigation for such systems. These materials include diamond [15], silicon carbide [16] and gallium arsenide [17], among others. One group working with diamond used nitrogen-vacancy color centers to observe a coherence time of 0.6 s [18]. However, these nitrogen vacancies are difficult and expensive to produce. Coherence times are typically on the order of 10-100 μs for SiC [16, 19]. However, D.J. Christle *et al.* recently measured isolated electron spins in SiC to have coherence times on the order of one millisecond [20]. Silicon carbide is advantageous because it is cheap, abundant, and manufacturing techniques are fairly advanced. We investigate electron spin states found in silicon vacancy defects of SiC and measure their lifetimes for use as qubit systems.

An overview of our experiment is described in Chapter 2. We use a laser to excite the electrons, a static magnetic field in conjunction with resonant microwaves to equalize the spin state population, a cryostat to cool the sample, and a photodiode detector combined with a lock-in amplifier to measure the emitted photoluminescence from the sample.

1.2 Background

1.2.1 Coherence time

Electrons have an intrinsic property called spin. When discussing spin coherence times, there are three parameters of interest: T_1, T_2, and T_2^*. The first, T_1, describes the amount of time for electron spins to relax to their equilibrium state. In our case, this corresponds to the time it takes the spin states to align with the magnetic field after resonant microwaves equalize the spin population. The second, T_2, determines the rate at which spins dephase from each other in the direction perpendicular to the static magnetic field due to spin-spin interactions [21]. For example, a resonant microwave pulse can be used to rotate the spins to 90° from the static magnetic field. Immediately after the pulse, the spins will not only begin to relax and align with the static field again, but the spin states perpendicular to the field will precess. These two processes are completely separate from each other. Due to the crystal structure of the material, the perpendicular precession rate will be different for each electron. These different rates will cause dephasing to occur, and eventually there will be no net spin in that direction. Once again, this is due to properties inherent in the material alone.

Finally, T_2^* also characterizes the time at which dephasing occurs in the direction perpendicular to the static field, but it takes into account inhomogeneities in the material as well. Therefore T_2^* is not as useful as T_2 because it is not a true limit of the coherence time. Inhomogeneities can be overcome using techniques like spin echo, which we employ. We wish to calculate the true limit to the coherence, T_2, and throughout the rest of this paper T_2 will be referred to as the spin lifetime.

1.2.2 Spin resonance

The orientation of electron spins can be probed along one direction to determine if the electrons are spin up or spin down. Orientation is normally random, but the energies of the spin states split

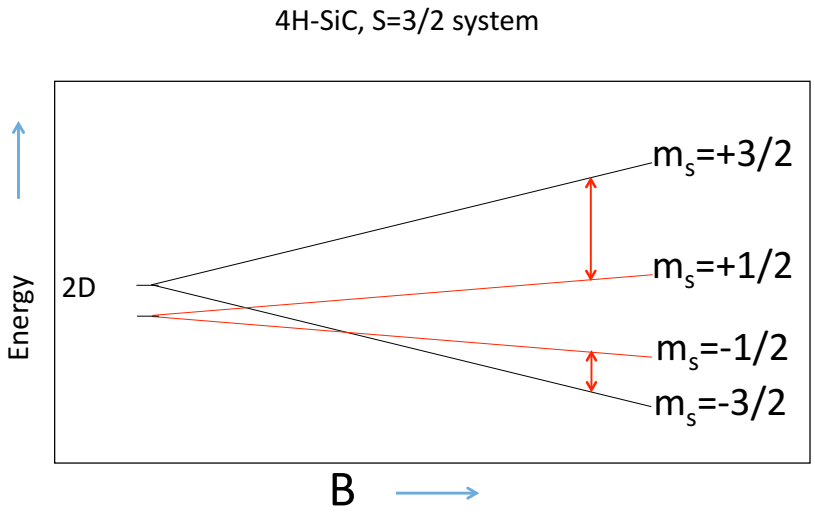

Figure 1.1 Spin $\frac{3}{2}$ system of electrons in silicon carbide. Energies vary linearly with the magnetic field. The red arrows are radiative transitions between spin states that can be bridged with resonant microwaves.

apart in the presence of an external magnetic field. An electron with spin parallel to the external field has lower energy than an electron with antiparallel spin. In addition, the difference between this energy gap increases with the applied field. The equation governing the energy difference in a spin $\frac{1}{2}$ system is

$$\Delta E = g_e \mu_B B_0, \tag{1.1}$$

where g_e is the electron spin g-factor for free electrons ($g_e \approx 2$, characterizes electron magnetic moment), μ_B is the Bohr magneton, and B_0 is the external magnetic field.

Electrons localized at the silicon vacancy defect in SiC make up a spin $\frac{3}{2}$ system [22], and as shown in Fig. 1.1 have four spin states. The energies of these states vary linearly with an external magnetic field. For a typical magnetic field in the laboratory (usually less than 1 tesla), the energy difference between these two states corresponds to a photon in the microwave frequency range. The microwave radiation with the exact same energy that splits the spin states is resonant with the spins. By applying waves of this frequency to the electrons, the spin states can be forced to change

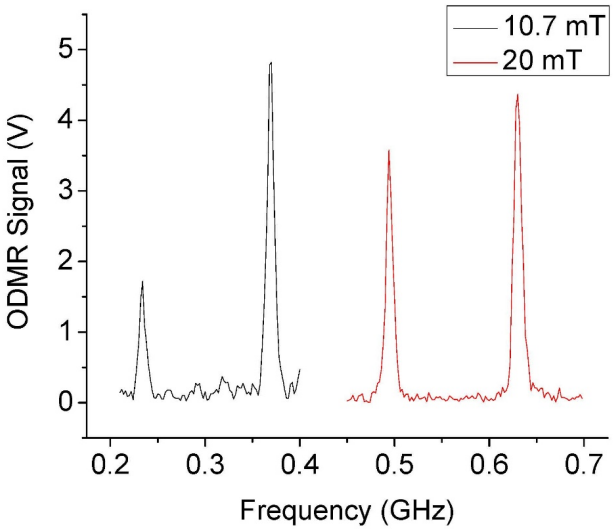

Figure 1.2 Typical spin resonance curve. The two peaks shown for each magnetic field correspond to the two red arrows showing transitions in Fig. 1.1. The resonance frequency for each peak varies linearly with magnetic field. The y axis is the optically detected magnetic resonance (ODMR) signal.

their state from spin up to spin down, or vice versa. Low energy electrons will absorb a photon to get to the high-energy state, and high-energy electrons will be stimulated to emit a photon and drop to the low energy state.

Not only microwaves with the exact same energy as the gap between the states will induce transitions, but also microwaves within about 20 MHz of the resonance frequency. This is because the transition occurs in a finite amount of time, and an uncertainty in time corresponds to an uncertainty in energy. Holding the field constant while varying the microwave frequency will produce a resonance curve that characterizes the system. This is the principle behind electron spin resonance. A typical spin resonance curve appears in Fig. 1.2. The two resonance peaks in this figure correspond to the top (i.e., $m_s = +\frac{3}{2} \rightarrow m_s = +\frac{1}{2}$) and bottom (i.e., $m_s = -\frac{3}{2} \rightarrow m_s = -\frac{1}{2}$) spin transitions. We usually work with the peak corresponding to higher energy microwaves in our experiments. However, we did not find any major difference between using one peak over the other.

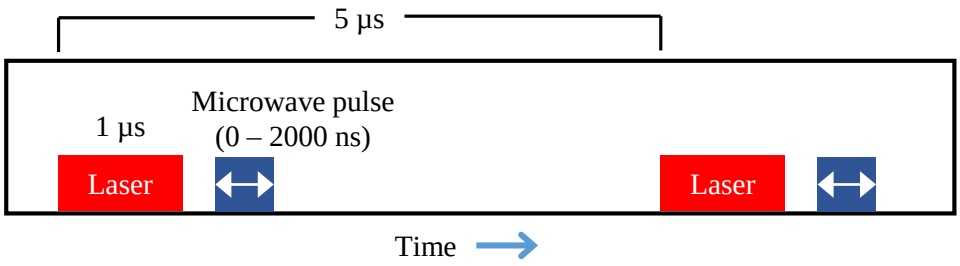

Figure 1.3 Timing schematic of laser and microwave pulses used to observe Rabi oscillations. Electron states are optically pumped into a high-energy state, then a duration-varied resonant microwave pulse causes the electrons to oscillate between spin states.

When the microwave power is increased, the height of each resonance peak also increases. Likewise, the peak height diminishes along with the peak width for lower microwave power. However, at very low power the peak no longer retains a Gaussian form, but it reaches a minimum width. Using the energy-time uncertainty principle, the frequency (i.e., energy) spread of the narrowest peak can give a rough value for the T_2^* coherence time.

1.2.3 Rabi oscillations

Once we have established a resonant microwave frequency, we then continue to operate at that frequency to observe Rabi oscillations. This technique determines the amount of time that it actually takes to switch an electron from one state to another. We can also observe dephasing of the electron spins states. This is done with pulse sequences of the laser and resonant microwaves.

First, spin states are preferentially populated by optically pumping all the electrons into the high-energy spin state (antiparallel with the magnetic field). In our experiment, this is done with an 870 nm laser. The laser also serves to stimulate PL, which allows us to measure the current spin state. After the laser pulse, a pulse of resonant microwaves is delivered to the sample. The duration of this pulse is varied. This pulse schematic can be seen in Fig. 1.3. From the photoluminescence (PL) of the sample we can determine the population of the spin states. As we increase the duration

of the microwave pulse from zero, we will reach the point when the majority of the spin states have been flipped into the opposite state. Further increasing the pulse length by the same amount will result in the majority of the states flipping back into their original state. Spins are thus flipped back and forth by longer and longer pulses. However, dephasing occurs while flipping the spins back and forth, causing the signal strength to decay exponentially. This decay time is given by T_2^*.

1.2.4 Spin echo

As discussed in Section 1.2.1, the goal of spin echo is to determine T_2, commonly known as the spin coherence time. We want to measure T_2 in a variety of samples and experimental conditions to discern which systems have long coherence times. This process utilizes microwave pulses of different duration: the π and the $\frac{\pi}{2}$ pulses. It is useful to think of the different spin states as being located on a sphere, with spin up directed vertically upward and spin down directed vertically downward. As implied by their names, the π pulse flips the spins from one state to another (from spin up to spin down, or 180°), while the $\frac{\pi}{2}$ pulse flips the spins halfway between spin up and spin down (90°).

A schematic detailing spin echo is displayed in Fig. 1.4. In the figure, the two times separating the pulses are both labeled as t. In practice, one often holds the first time delay fixed and varies the second time delay, so we refer to them as T_{fixed} and τ, respectively. The pulse sequence begins with a $\frac{\pi}{2}$ pulse that rotates the spins 90°, as seen in Fig. 1.4 (B). Due to spin-spin interactions and field inhomogeneities, the spins begin to dephase at unequal rates. Shown in Fig. 1.4 (C)-(D), a π pulse applied a time T_{fixed} later flips the spins 180°. Figure 1.4 (E)-(F) shows the spins phasing back together. This occurs because the spins precessing slowly now lead the spins that were precessing quickly. Each spin continues to precess at its original rate to combine back together. A final $\frac{\pi}{2}$ pulse rotates the spins 90° back to their initial state (not shown in the figure). The degree to which the original spin population is preserved gives the spin echo. The spin echo is only observed if

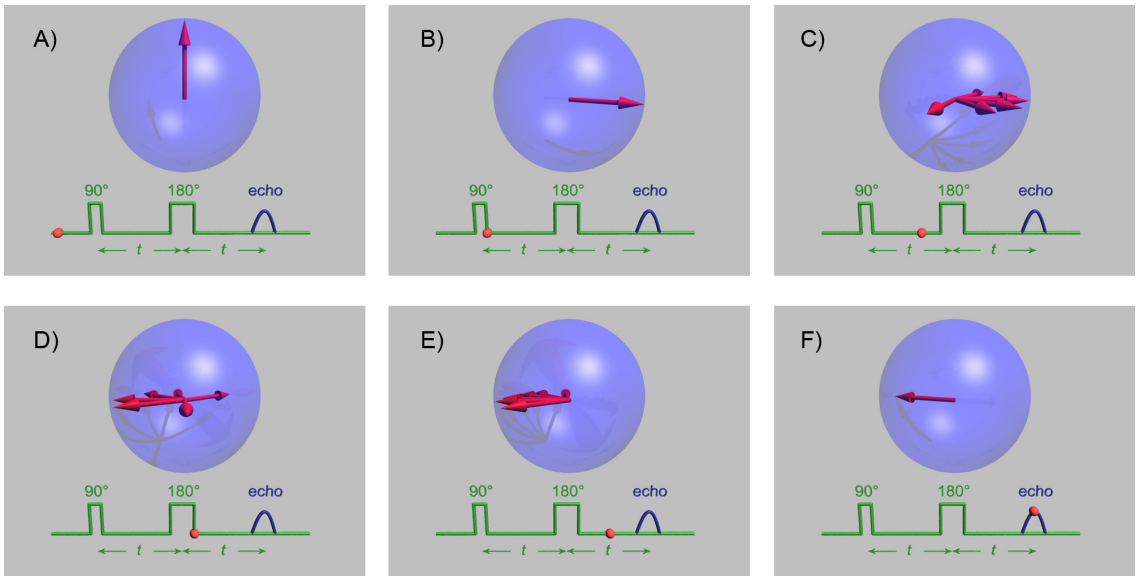

Figure 1.4 Schematic of electron spin states during a spin echo experiment [23]. (A) Spin states are aligned in the vertical direction. (B)-(C) A $\frac{\pi}{2}$ pulse rotates spin states by 90°, after which they begin to dephase. (D)-(E) A π pulse rotates the spins 180°, after which they begin to phase together again. (F) The echo signal is observed from the recombined spin states and is proportional to the overall coherence. Not pictured in this figure is the last $\frac{\pi}{2}$ pulse we use to flip the spins another 90° into the vertical position.

the last $\frac{\pi}{2}$ pulse is delivered when the spins have precessed back together completely. This occurs when the time between the last two pulses, τ, is the same as T_{fixed}, the time between the first two pulses.

This delay between the last two pulses, τ, can be varied across a range of values centered on T_{fixed}. When $\tau = T_{\text{fixed}}$ the spin echo signal is maximized as the electrons are returned to their initial spin state. After varying τ to observe the spin echo, a new T_{fixed} is set and the scan is repeated. As T_{fixed} is made larger and larger, more randomization occurs within the electron spin states before recombining, and the spin echo signal becomes weaker. The spin echo decay is typically exponential, characterized by a decay time whose value is T_2. As mentioned before, this property is the true limit of the spin coherence time. Therefore, it is important to analyze a variety of samples and experimental conditions to find a system with a long T_2.

1.3 Silicon carbide as a spintronic device

1.3.1 Previous work

Other research groups have worked at room temperature to characterize coherence times in SiC [24], but our work explores the effect of temperature on the lifetimes. In addition, we explore defect type and concentration in an effort to maximize the lifetime. Sam Carter and collaborators at the Naval Research Laboratory have characterized silicon defects in 4H SiC specifically at room temperature [19]. They found a large dependence of the coherence time on magnetic field. However, they have only measured coherence times of electron-irradiated SiC, and we are measuring both electron and proton-irradiated SiC.

1.3.2 Silicon carbide samples

We currently work with three different silicon carbide samples: 10^{13} cm^{-2} proton-irradiated, 10^{14} cm^{-2} proton-irradiated, and 10^{17} cm^{-2} electron-irradiated. All samples are made from 4H SiC [25]. Silicon vacancy defects were created through irradiation with either protons or electrons in the amount specified. Most of this work was done by Brad D. Weaver and Evan Glaser at the Naval Research Laboratory. The irradiation was done only from one side of each sample, and it is estimated that the defects occur about 30 μm deep into the surface. We suppose that the nature of the defects is different whether formed by proton or electron irradiation. In addition, we investigate how the density of defects affects the coherence time.

1.3.3 Summary of results

In our experiments, we have found no correlation between the spin coherence time and temperature. We took data at five different temperatures between 6 K and room temperature (see Section 3.2). While the signal to noise ratio was much improved for temperatures below about 80 K, the coherence time seemed to remain the same. However, defect concentration dramatically affected T_2. Reducing the defect concentration by a factor of 10 increased the coherence time by more than a factor of three in proton-irradiated SiC. Defect type also affected the data, but we were only able to put a lower limit on the lifetime in electron-irradiated SiC. In addition, Rabi oscillations did not appear very clearly in the data, and we presume this is because of a short T_1 which damps these oscillations very quickly.

1.3.4 Organization of thesis

Chapter 2 will discuss the experimental setup, as well as specific procedures to operate some of the equipment. Several problems were overcome to maximize the microwave power delivered to the

sample and to reduce the overall noise in the experiment. Following the experimental procedures, Chapter 3 presents results for the spin resonance, Rabi oscillation, and spin echo experiments. We form conclusions from comparing the data to expected results. In addition, we will examine the effects of varying conditions of the experiment (e.g., laser wavelength, microwave power, temperature and defect concentration). Based on these results, we present ideas for future research.

Chapter 2

Experimental Setup

A spin-resonance experiment requires extensive coordination between equipment. In our setup, we faced several challenges with equipment coordination. First, a pulsed laser must be synced in time with pulses of microwave radiation just tens of nanoseconds in duration. Second, a coupling loop placed close to the sample needs to be impedance-matched to allow successful delivery of high-power microwaves. Third, the magnetic field must be precisely controlled to within fractions of a millitesla. These challenges necessitate careful design and orientation of equipment. This chapter focuses on the layout, design, and techniques used to coordinate the many separate components of this experiment.

2.1 Optical setup

First we discuss the optical setup of the experiment. A general schematic can be seen in Fig. 2.1. The photoluminescence (PL) of interest emitted by the sample is about 915 nm, so the laser light used to excite this PL must be at or below this wavelength. After experimenting with various wavelengths, we chose 870 nm light to interact with the spins in the silicon vacancies. This was chosen because we observed that the signal-to-noise ratio increases with wavelength, but we also

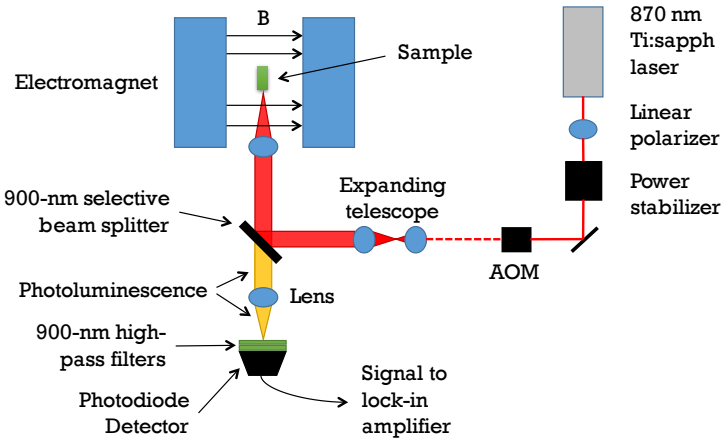

Figure 2.1 Schematic of optical setup. The titanium-sapphire (Ti:sapph) laser is excited by a 532-nm laser (not shown here) emits light at 870 nm. The linear polarizer is necessary for the power stabilizer. The acousto-optic modulator (AOM) gates the laser on and off to form pulses, and is followed by an expanding telescope. A 900-nm selective beam splitter reflects the laser (< 900 nm) towards the sample but allows the photoluminescence (> 900 nm) to pass through to the detector.

wanted the laser beam well-distinguished from the PL to be able to block it with a filter or beam splitter. This light is produced from a titanium-sapphire (Ti:sapph) laser driven by a 532 nm green laser. The green laser outputs at 5 watts, and the Ti:sapph produces about 1 watt of power. The output of this laser is linearly polarized, and it passes through a laser power controller to reduce noise.

To pulse the laser, we use an acousto-optic modulator (AOM). This is a crystal with a piezo-electric transducer attached. Applying a voltage to the crystal turns it into a diffraction grating. The crystal is designed such that the first-order diffraction beam contains about 72% of the total laser power. We block all but the first-order beam, which is only present when voltage is applied to the AOM. This allows us to pulse the laser using the applied voltage. The voltage can also be timed with the microwave pulses for the Rabi and spin-echo timing sequences, which are controlled by a PIN diode placed on the output of the microwave generator.

The spin states located in the silicon vacancies are most effectively pumped when the laser

intensity is high, so we desire a tight focus of the laser. Exiting the Ti:sapph, the laser beam is about one millimeter in diameter. Focusing this beam with a one-inch lens increases the intensity, but a much tighter focus is obtained by first expanding the beam to one inch, then focusing it down. Treating the laser beam as a Gaussian profile, we can derive an equation for the beam waist, or size of the beam at its smallest diameter [26]. This equation is

$$w_0 = \frac{2\lambda f^{\#}}{\pi}, \tag{2.1}$$

where w_0 is the beam waist and $f^{\#}$ is the f-number. The f-number is calculated by dividing the focal length of the lens by the diameter of the (parallel) beam prior to the lens. Thus by expanding the beam by more than a factor of 10 (to fill the one-inch lens), we decrease w_0 by a factor of 10, increasing the intensity by a factor of 100.

Information about the electron spins is collected by observing the photoluminescence (PL) emitted by the sample. We want to collect as much of this light as possible. However, because the sample is residing inside a cryostat, the viewing angle of the sample is limited to the size of the cryostat window. The PL exiting at other angles is lost. In addition, much of the 870 nm incident laser light is scattered backwards due to reflections off the cryostat window and the sample itself. Without any filtering, the laser light at the detector would be many orders of magnitude stronger than the PL. In order to compensate, a wavelength-selective beam splitter is used essentially as a 900-nm high-pass filter. It acts as a mirror to direct the incident laser light to the sample, but it also reflects the scattered laser light in a different direction. A lens is placed directly behind the beam splitter, followed by a photodiode detector. Due to the very small intensity of PL (just a few hundred nanowatts), two 900-nm high-pass filters are attached to the detector to block room light and any stray laser light. The entire schematic can be seen in Fig. 2.1.

The detector measures the intensity of the PL, but we are also interested in knowing its exact spectrum. The collecting lens and detector can be taken out of the beam path to direct the PL into a spectrometer on another table. Because the light coming from the sample is collimated, it can

travel a few feet without spreading out significantly. A 3-inch lens is then used to ensure collection of as much PL as possible. A charge-coupled device (CCD) is attached to the spectrometer, which quickly measures the spectrum of the emitted PL. Plots of the collected photoluminescence are shown in Section 3.1.1, where we discuss the changes in the spectrum with temperature and defect type.

2.2 Microwave pulse system

Microwave pulses as short as tens of nanoseconds must be delivered to the sample to detect Rabi oscillations and spin echo. These pulses must be coordinated with the laser pulses to correctly interact with the electron spins. In this section we discuss the implementation of a function generator, pulse generator, lock-in amplifier, and AOM to achieve this complex pulse sequence. In addition, we discuss problems with impedance matching of the microwave amplifier to the coupling loop that resulted in poor power throughput to the sample.

2.2.1 Timing

Rabi-oscillation experiments require a microwave pulse to be delivered a fixed amount of time after a laser pulse, and the duration of the microwave pulse must be varied. Spin echo requires three different microwave pulses to be delivered after a laser pulse, with different duration and time offsets. In addition, we take data with a lock-in amplifier to extract the signal from the experiment, which necessitates that the whole process be gated (i.e., microwaves turn on and off). A general schematic of how this timing is achieved can be seen in Fig. 2.2, where the role of the multiple instruments involved is shown. We employ two channels of a Tektronix function generator (FG) to supply the voltage to the AOM and to an Agilent pulse generator (PG), which in turn provides pulses that turn on and off the microwave generator.

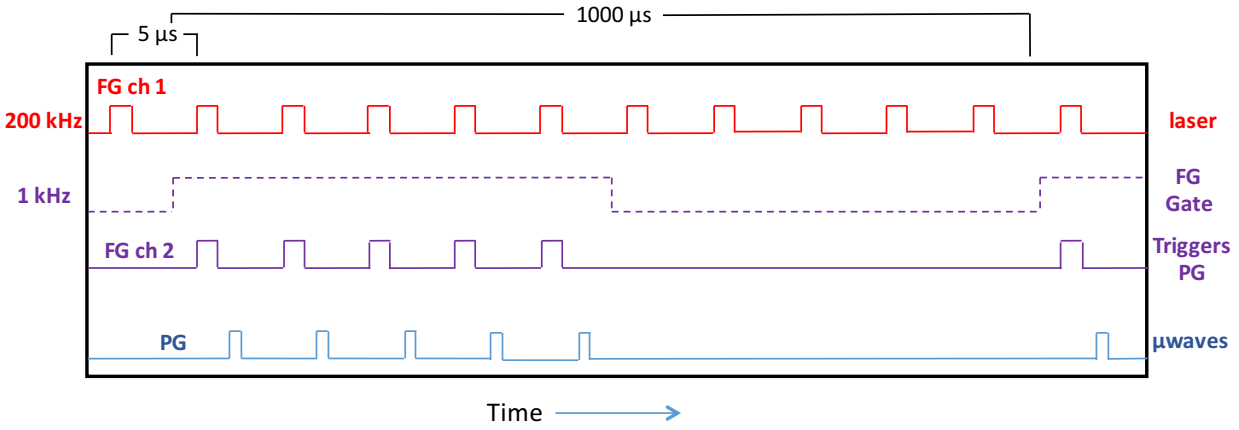

Figure 2.2 Timing schematic of the function generator (FG) and pulse generator (PG) to pulse the laser and microwaves, respectively.

The laser is pulsed constantly, and short microwave pulses follow each laser pulse. The goal is to turn the microwave pulses on and off at a lower frequency that can be detected by the lock-in amplifier. We refer to this low-frequency oscillation as a gate. The process begins with channel 1 of the function generator (FG), which turns the laser on and off. We typically operate this channel between 35 and 200 kHz, with a pulse width of 1 μs for the Rabi experiment and 2 μs for the spin echo experiment. This channel is only routed to the AOM, which causes the laser to pulse continuously. Channel 2 of the FG outputs a signal similar to channel 1, but it is gated at a rate of 1 kHz. This gate is achieved by an internal setting of the FG. Thus Channel 2 has both the fast oscillation found in Channel 1 and the low-frequency gate. The output from channel 2 triggers the pulse generator (PG). Once the PG is triggered, it initiates its own pulse sequence, which turns the microwaves on and off by means of a PIN diode. Care must be taken so that the time required to complete this sequence is less than the period of channel 1 on the FG (i.e., the entire microwave pulse sequence must fit between laser pulses). A schematic of the electrical setup can be seen in Fig. 2.3.

The trigger output of the FG contains the 1 kHz gate frequency, which is fed into the lock-in

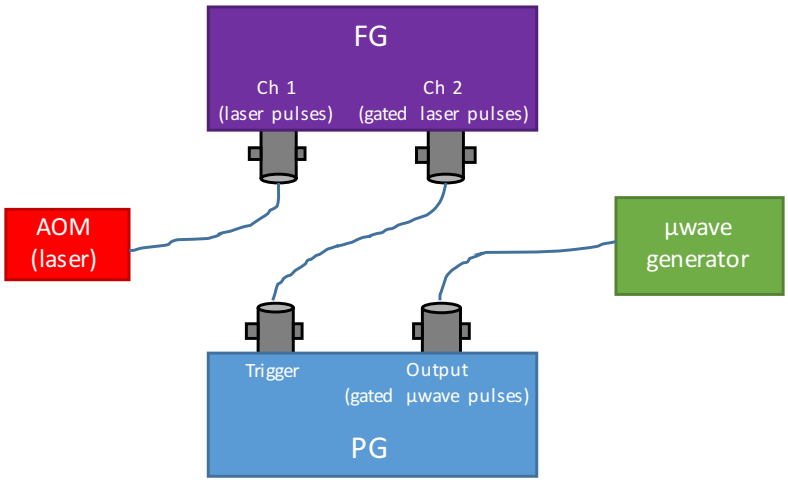

Figure 2.3 Schematic of electrical inputs and outputs. The function generator (FG) has two output channels. Both contain the laser pulse sequence, but channel 2 is also gated at a lower frequency of 1 kHz. The acousto-optic modulator (AOM) controls the laser pulses. Channel 2 is the trigger input to the pulse generator (PG). The output of the PG goes to the microwave generator and controls the microwave pulse sequence.

amplifier. Having the gate applied only to the PG output means that the laser is always pulsing on and off, but the microwave pulse sequence is only happening 50% of the time. This is useful because it enables us to extract the information that is only pertinent to spin interactions. The sample will always emit PL when exposed to the laser, but the intensity of the PL changes based on the interaction between microwaves and spins. The lock-in amplifier ignores signals at frequencies other than 1 kHz, allowing us to observe the effect the resonant microwaves alone have on the PL and ignore the pulsing laser light.

2.2.2 Impedance matching

As was mentioned in Chapter 1, Sam Carter [19] has taken data with some of the same samples that we are using. After comparing our data to his, we noticed that our actual microwave power was considerably less than what we thought it should be. Through a lot of trial and error, we discovered that the impedance of our microwave amplifier output terminal was not matched to the impedance of the coupling loop in front of the sample. We then used a network analyzer to determine the characteristics (e.g., impedance, frequency response, resonance, etc.) of the coupling loop and cable system.

Without much flexibility in cable length (a coax cable extends about five feet down through the cryostat), tuning the impedance of this circuit involved using a stub tuner, also known as a "slide trombone." Stub tuners are essentially a variable-length cavity that can be attached in parallel to a coaxial cable. To be effective, they must be on the order of a quarter wavelength long. We normally use microwaves with a frequency of about 10.5 GHz, which equates to a wavelength of roughly 3 cm. The stub tuners that we used were around 10 cm long, and we could easily adjust their length until the microwave power was maximized. We measured the microwave power with a separate pick-up loop situated just outside the cryostat window. This loop was hooked to a directional coupler, and the power was measured with an oscilloscope. Using the sweep feature of

our microwave generator, we could measure the power output at various frequencies. With real-time adjustment of the stub tuner length we maximized the power output at a specific frequency. More information on radio-frequency impedance matching can be found in other papers [27, 28].

2.3 Magnetic field

A stable magnetic field is crucial for a spin-resonance experiment. Detecting both Rabi oscillations and spin-echo data relies on using microwaves resonant with the electron spin state transitions. Because these energies depend on magnetic field, control of the field must be both precise and stable. In our experiment, we use a large Varian magnet with an impedance of about 1024 Ω. We recently bought a new power supply to power the magnet, and I wrote LabVIEW code to interface with it. While coding for the power supply, I learned how to achieve a stable and precise field, and I present those facts in the rest of this section.

The Magna Power supply has both constant voltage and constant current modes. The magnetic field is dependent on the current, so originally we operated the power supply in constant current mode. However, stability was poor in this mode. When giving digital commands to the power supply, it was difficult to obtain a field step size small comparable to a resonance peak width for a particular microwave frequency. The stability was improved in constant voltage mode, but we still faced problems with too small of a step size. In addition, temperature changes affected the resistance of the magnet and caused the field to drift over time.

To solve these problems, we tried controlling the power supply by another method. In addition to a digital input, the Magna Power supply can take an analog input between 0 and 5 volts, which it then scales to determine its output voltage. We devised a variable resistor network that included a potentiometer to vary the voltage by smaller increments. This worked fairly well to reduce the step size of the magnetic field, since a potentiometer has essentially infinite resolution. However,

the resistors were very susceptible to changes in temperature as well as small movements and vibrations, making them an inadequate solution to this problem. Finally, we began using a Fluke 5100B voltage calibrator to supply the analog voltage to the power supply. This voltage calibrator has seven significant digits, enabling the variation of the analog voltage down to 1 μV. With this calibrator, we were able to control the magnetic field with a precision of about 10 μT. Temperature changes in the magnet remain problematic, but the field drifts caused by this effect are relatively small if the magnet is left to stabilize for about two hours before any experiments are done.

Chapter 3

Results and Conclusions

In this chapter we present the data obtained from the spin resonance experiments. We discuss the temperature dependence of the lifetime, which was minimal. We also present the variation of lifetime with defect concentration and type, which was significant. Decreasing the defect concentration in proton-irradiated SiC appears to lengthen the lifetime. The electron-irradiated sample has a longer lifetime than the proton-irradiated samples, but we were only able to put a lower limit on it.

3.1 Spin resonance data

3.1.1 Photoluminescence

In this section we compare the photoluminescence (PL) of the different samples at various temperatures. This data is obtained simply by examining the light emitted from the sample with a CCD camera through a spectrometer. The PL for multiple samples can be seen in Fig. 3.1. The incident laser power was about 0.7 W at the sample for each plot, and the laser was focused on the edge of the sample for each trial. The CCD was used with ten averages and an integration time of 100

ms. In all cases, the peak of interest is the left-most peak found in the spectra, located at about 915 nm. This is known as the V2 spectral line, and it is this line that relates to electron transitions in the silicon vacancy defect. At low temperatures, the V2 line, among others, are very sharp and well-defined peaks [29]. However, at higher temperatures the peaks broaden out and begin to blend with one another.

Another important feature is the relative strengths of the PL between the two different samples. It is roughly four times stronger for the 10^{14} cm^{-2} proton-irradiated sample than it is for the 10^{13} cm^{-2} proton-irradiated sample. This is because the defects give rise to the spectral peaks, and a higher density of defects causes a higher intensity of PL. However, the exact ratio between intensities in these two graphs should not be taken as exact. The strength of the PL varies depending on the location of the laser spot as well as the optical alignment going into the spectrometer. These variations can cause the PL to change by a factor of about 1.5, and more rigorous testing would be needed to determine the exact ratio of intensity between the two samples.

3.1.2 Optically detected magnetic resonance

To perform the spin echo experiment and determine the electron spin lifetime, resonance must first be reached. The correct frequency of microwaves must be determined for a specific magnetic field (or vice-versa) to allow for electron spin transitions. The easiest way to determine this resonance condition is to set the magnetic field, then sweep through microwave frequencies until a resonance peak is seen. Because 4H-SiC is a spin $\frac{3}{2}$ system, there are actually two resonance peaks. One corresponds to a transition between the $m = +\frac{3}{2}$ and $m = +\frac{1}{2}$ states, and the other corresponds to a transition between the $m = -\frac{1}{2}$ and $m = -\frac{3}{2}$ states. A typical microwave frequency scan that unveils these two resonance peaks was shown in Fig. 1.2. In our further measurements, we typically focus on the uppermost peak.

We are also interested in the percent change in the PL when at the resonance peak, which we

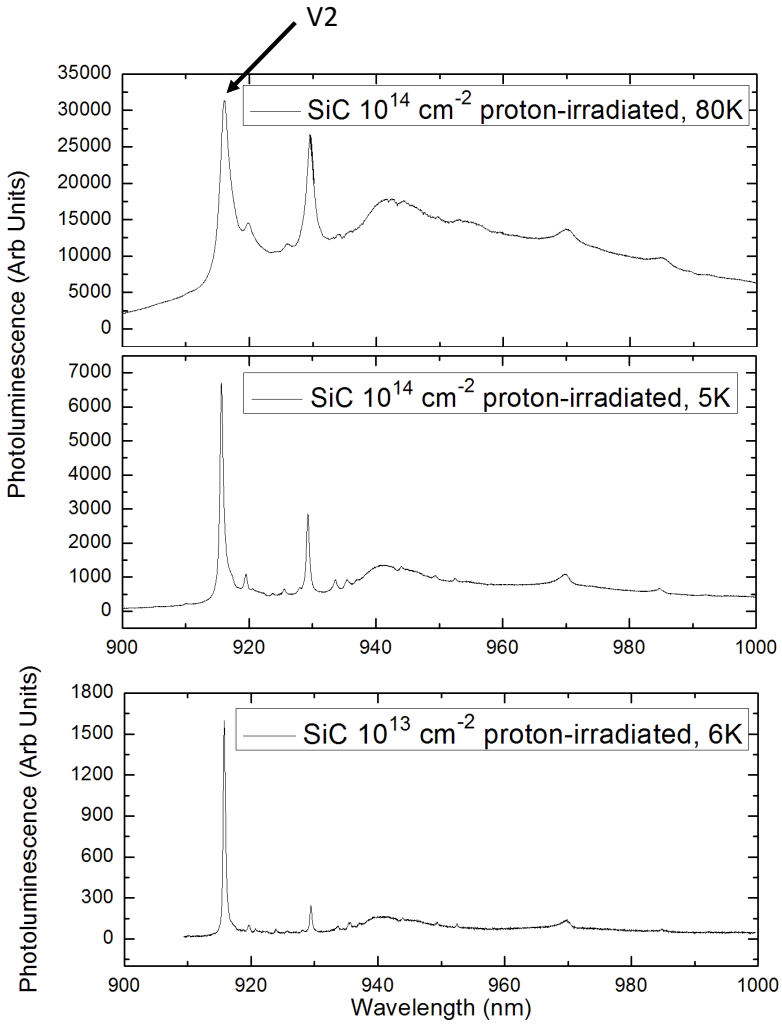

Figure 3.1 Photoluminescence (PL) of various samples of SiC at different temperatures. Note the increased strength of the spectral peaks for the 10^{14} cm^{-2} proton-irradiated sample over the 10^{13} cm^{-2} proton-irradiated sample. In addition, the peaks tend to broaden out and blend together at higher temperatures.

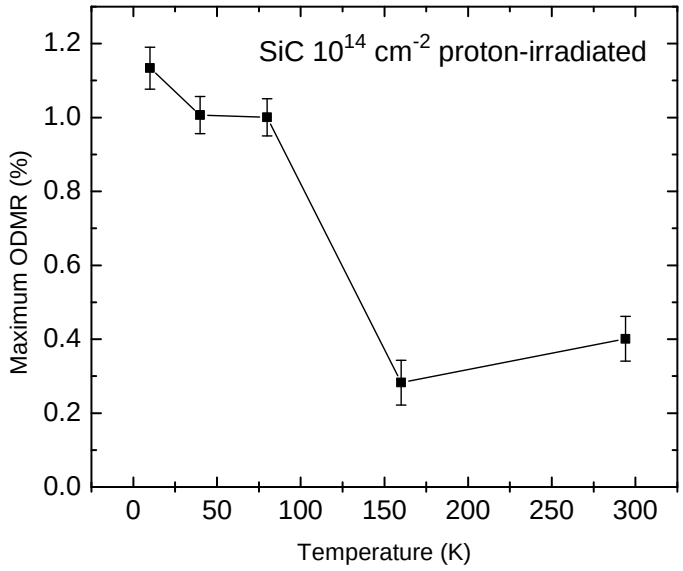

Figure 3.2 Percent change in the PL when at the resonance peak (% ODMR). The higher the % ODMR, the better signal-to-noise ratio for collecting data. We see an increase in % ODMR at low temperatures, allowing for cleaner data in general.

will call percent optically detected magnetic resonance (% ODMR). This is calculated by comparing the signal on the lock-in when chopping the resonant microwaves to the signal when chopping the laser itself. The higher the % ODMR, the higher the signal-to-noise ratio. As can be seen in Fig. 3.2, this number is higher at lower temperatures. This is perhaps due to the narrowing of the spectral peaks at low temperatures. At any rate, it makes collecting data at lower temperatures easier than at room temperature.

3.1.3 Rabi oscillations

As explained in Section 1.2.3, resonant microwaves cause electron spin states to oscillate between spin up and spin down states. The frequency of these oscillations depends directly on the strength of the incident microwave field. However, these oscillations are damped by a decaying exponential

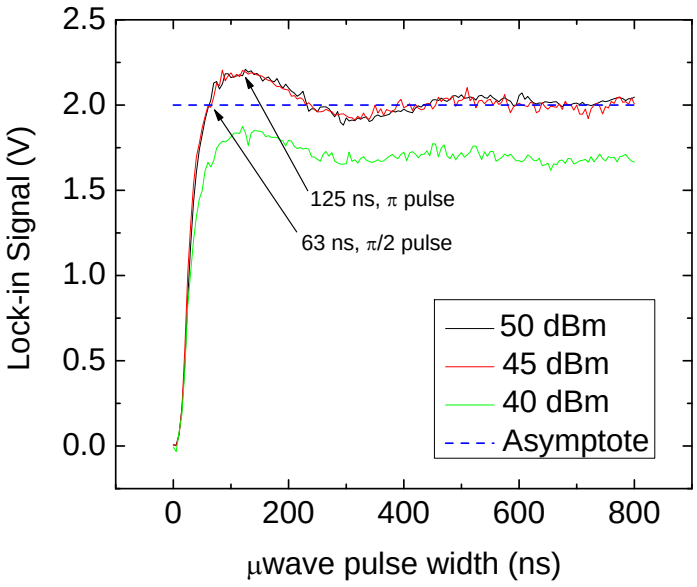

Figure 3.3 Rabi oscillations for the 10^{14} cm^{-2} proton-irradiated sample. The oscillations are not well defined and die off quickly, possibly due to a small T_1 value.

with a time constant equal to T_2^* [30]. If this relaxation time is too short, the oscillations won't be seen at all. Relaxation occurs because the electrons dephase too quickly. In the samples we tested, it proved difficult to collect data showing clear Rabi oscillations. Figure 3.3 shows the clearest data we have for any of the samples. This data was collected from the 10^{14} cm^{-2} proton-irradiated sample, and scans were taken at three different microwave field strengths. We notice there is not much difference between the 45 dBm and 50 dBm curves, indicating that the microwave amplifier is not changing its output between these two settings.

The duration of the $\frac{\pi}{2}$ pulse is obtained from the point where the increasing lock-in signal first reaches the asymptotic value of the signal. The π pulse duration is obtained at the peak of the lock-in signal. These locations are pointed out in Fig. 3.3. When there were no oscillations in the Rabi signal (other than the original spike), the $\frac{\pi}{2}$ pulse duration can be estimated to where the lock-in signal first reaches a value that is slightly less than the asymptotic value. Usually the $\frac{\pi}{2}$

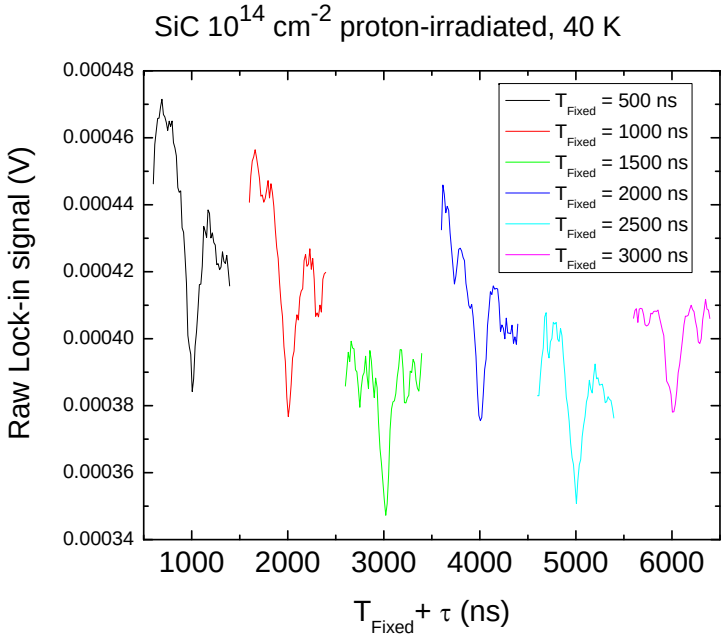

Figure 3.4 Raw spin echo data. Notice that each peak has a different overall slope, and the overall height decreases with delay time. The laser pulse width was 2 μs, and the overall period varied between 5-10 μs for the various scans.

pulse length is between one-half and two-thirds of the π pulse length. To improve the Rabi signal, the oscillations can be magnified by re-centering the field at resonance, choosing different lock-in time constants, or by refining the focus of the laser.

3.1.4 Spin echo

For a review of the terminology used here, see Section 1.2.4. When sweeping through the second $\frac{\pi}{2}$ pulse delay time, τ, the PL intensity changes when $\tau = T_{\text{fixed}}$. This occurs when the delays between the first and second pulses, as well as the second and third pulses, are the same. When spin echo data is initially taken, it looks like an upside-down Gaussian. Figure 3.4 shows an example of raw spin echo data for various delay times, T_{Fixed}. Because the delay between pulses becomes longer with each scan, the total laser power decreases with longer values of T_{fixed}. This generally causes each subsequent data set to have less signal. Changing the alignment or re-tuning the magnetic

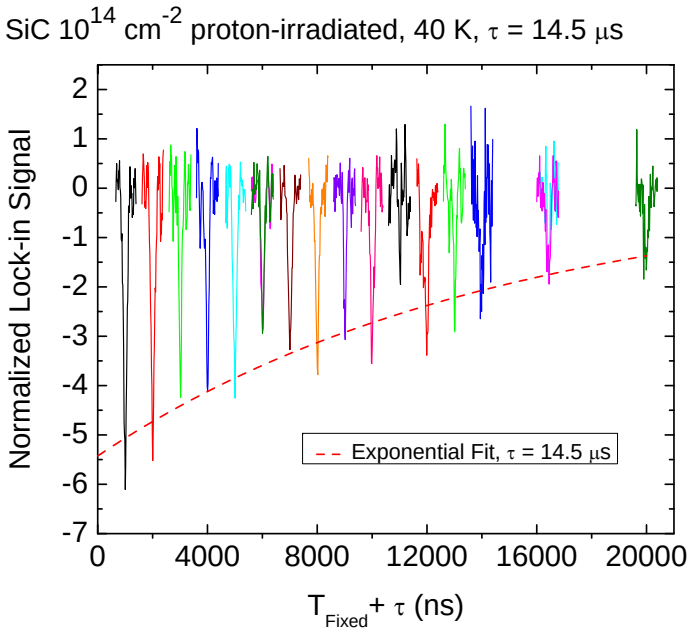

Figure 3.5 Spin echo data with the linear baseline offset removed from the raw spin echo data. This data is from the 10^{14} cm^{-2} proton-irradiated sample. The peak heights exponentially decrease toward zero. The decaying peak heights are fit to give the T_2 relaxation time. $T_{\text{fixed}} + \tau$ represents the total delay time between the first and last pulses in the sequence. To compensate for the overall decreasing signal strength in successive data sets, each curve was first multiplied by a constant so the top portion of the data was about the same value as the top of the first data set (i.e., the black curve in Fig. 3.4).

field to resonance can change the signal strength from one trial to the next, but the overall trend is a decreasing signal. There are two ways to correct for this problem. The first is shown in Fig. 3.5. Each curve is first multiplied by a constant so the top portion of the data is about the same value as the top of the first data set (i.e., the black curve in Fig. 3.4). A linear baseline is then subtracted from each data set. As seen in Fig. 3.5, the peak heights decrease as the delay time becomes longer. The peak heights are then fit to an exponential decay, and the time constant in this decay yields T_2. This exponential fit is shown in Fig. 3.6.

The second way, which we found to be the better method, is to fit the data to a Gaussian shape with a linear offset term. Such a fit can be seen in Fig. 3.7. The linear offset takes into account

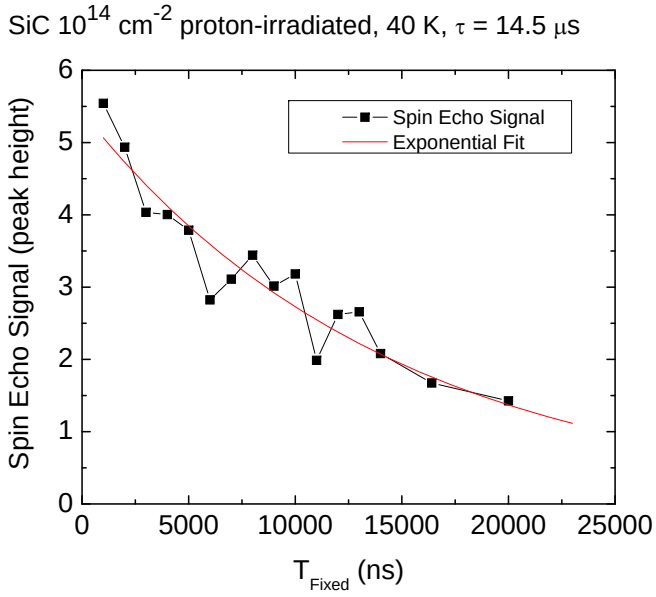

Figure 3.6 Spin echo signal for 10^{14} cm^{-2} proton-irradiated SiC using the linear baseline removal. The spin echo signal, or height of each peak from Fig. 3.5, is fit to an exponential decay whose time constant is T_2.

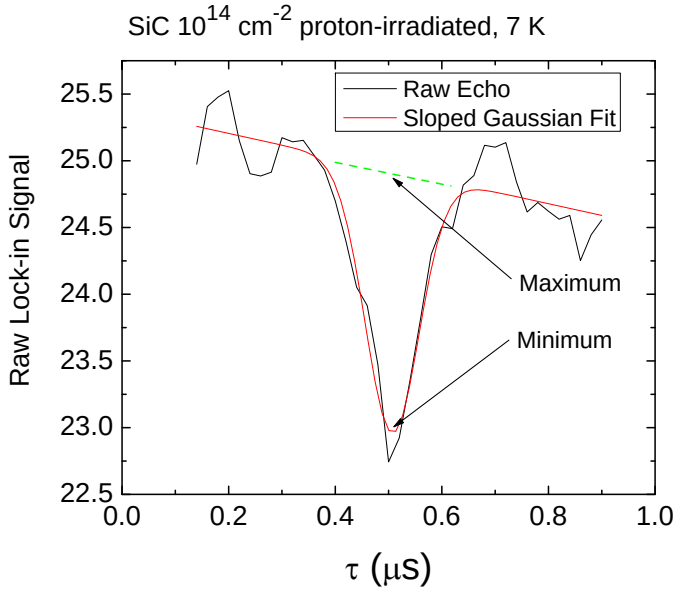

Figure 3.7 One segment of raw spin echo data fit to a Gaussian shape with a linear offset. The data was taken from the 10^{14} cm^{-2} proton-irradiated sample at 7 K. The spin echo signal, or percentage change of the PL, is calculated from this fit using $100 \times (1 - \frac{\text{Minimum}}{\text{Maximum}})$.

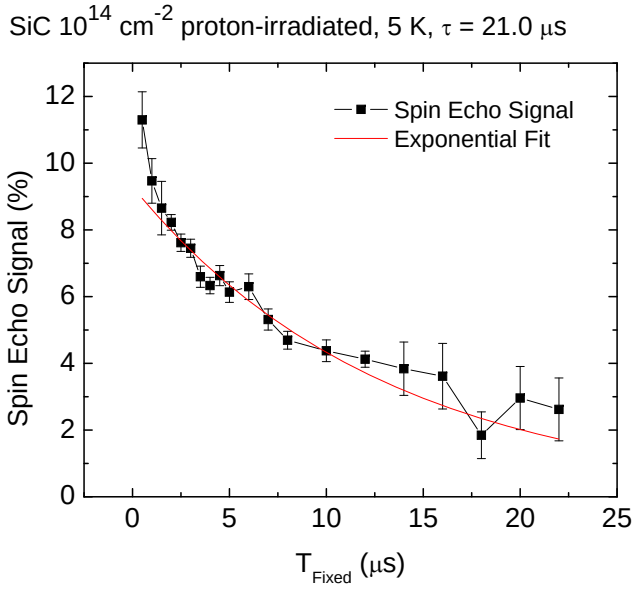

Figure 3.8 Spin echo signal for 10^{14} cm^{-2} proton-irradiated SiC using a Gaussian fit on the raw echo data. The spin echo signal, or percentage change of the PL, is fit to an exponential decay whose time constant is T_2.

small drifts in the field over the course of a scan. The spin echo signal is the percentage change in the PL. We calculate this by taking the ratio of the lowest point on the Gaussian to the point above it on the baseline alone, or $100 \times (1 - \frac{\text{Minimum}}{\text{Maximum}})$. By using a ratio, this takes into account the decreasing laser power for each successive scan. It is the preferred method because the ratio more accurately compensates for the changing laser power than the other method. This technique was used on all spin echo data taken to determine the spin echo signal. The time constant of an exponential fit to the spin echo data then gives the T_2 lifetime. Figure 3.8 shows the fit that results from using this method for fitting the same data that has been shown in Figs. 3.5 and 3.7.

3.2 Temperature dependence

Initially we thought temperature would have an effect on the spin lifetime. We extensively tested the 10^{14} cm^{-2} proton-irradiated sample at five different temperatures, but the lifetime appears to

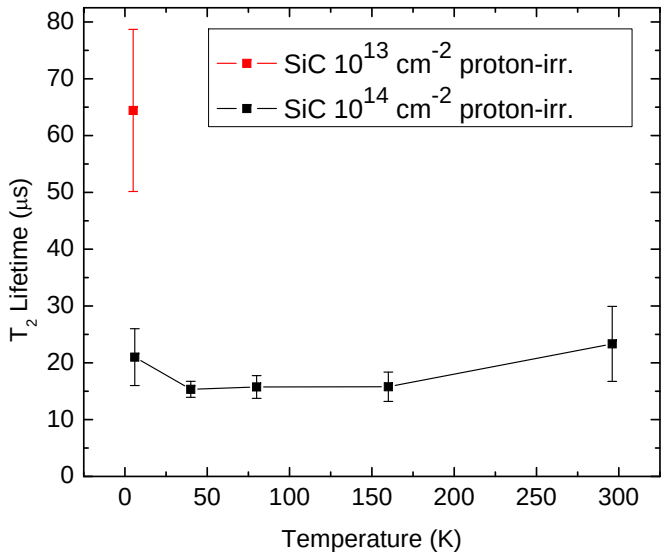

Figure 3.9 Comparison of defect concentration on the T_2 spin lifetime with 10^{13} cm^{-2} and 10^{14} cm^{-2} proton-irradiated samples. Though rather constant with temperature, lifetime is substantially larger for the sample with fewer defects. Also, data taken at lower temperatures contains less noise.

remain rather constant. In Fig. 3.9, the lifetime can be seen to be about 17 μs over a broad range of temperatures for the 10^{14} cm^{-2} proton-irradiated sample. However, the noise is substantially reduced when taking data at lower temperatures (except for an anomaly at 5 K), allowing for increased accuracy in estimating the lifetime. We expect this is due to the narrowing of the V2 line observed in the spectrum of the PL at low temperatures. The increased noise at 5 K could be due to an alignment problem of the laser spot, or possibly due to a bi-exponential decay process. If the system actually has two lifetimes, this might show up as extra noise.

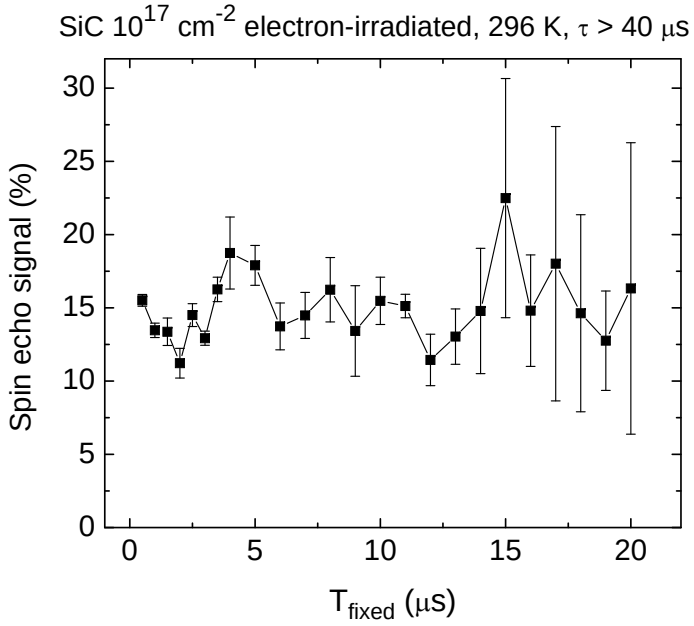

Figure 3.10 Spin echo signal for 10^{17} cm^{-2} electron-irradiated SiC. Note the absence of an exponential decay in the signal. We can only estimate a lower limit of the spin lifetime.

3.3 Dependence on defect concentration and type

We have observed that the spin lifetimes vary drastically with defect concentration and type. We determined the effect of defect concentration by measuring the spin lifetime in the 10^{13} cm^{-2} and 10^{14} cm^{-2} proton-irradiated samples. Because of the limited PL emitted from the sample with fewer defects, there is more noise and uncertainty in the lifetime measurement. However, we can still see in Fig. 3.9 that the sample with fewer defects has a longer lifetime. One possibility is that extra damage or defects are found in the 10^{14} cm^{-2} proton-irradiated sample. There could be an overall loss of spin info when the electrons get scattered by regions with structural damage. Another possibility is that because of the large amount of radiation, silicon vacancy defects are so frequent that significant cross-talk between defects leads to spin info loss.

Next we show the effect of defect type on the spin lifetime. To do this we collected spin echo data on a 10^{17} cm^{-2} electron-irradiated sample. Figure 3.10 shows a substantial difference in echo

Temp (K)	10^{13} cm^{-2} proton	10^{14} cm^{-2} proton	10^{17} cm^{-2} electron
6	64.4	21.0	—
40	—	15.3	—
80	—	15.7	—
160	—	15.8	—
295	—	23.3	>40

Table 3.1 T_2 spin lifetimes of various silicon carbide samples at different temperatures. All lifetimes are in units of μs. The labels "proton" and "electron" denote proton-irradiated SiC and electron-irradiated SiC, respectively. We observe lifetimes that are fairly independent with temperature, decreasing with defect concentration, and largely undetermined for the electron-irradiated sample. The blank entries in the table are data we have not yet taken, but plan to take soon.

signal with this sample compared to the others. There really doesn't seem to be any decay in the spin echo signal over the 20 μs region we tested, although it is difficult to judge given the increased noise at longer delay times. However, we can put a lower limit of 40 μs on the T_2 lifetime for this electron-irradiated sample.

A summary of the all spin lifetime data can be seen in Table 3.1. This information is presented graphically in Fig. 3.11. The only sample for which we took data at all five temperatures is the 10^{14} cm^{-2} proton-irradiated sample. We include the other samples in the table because we intend to take data at various temperatures for those samples as well, but have not yet done so.

3.4 Conclusions and future work

The 10^{13} cm^{-2} proton-irradiated sample appears to have a much longer lifetime than the more highly irradiated 10^{14} cm^{-2} proton-irradiated sample. We are possibly looking at defects other than just silicon vacancies in the 10^{14} cm^{-2} sample. The depth of defects is on the order of 30 μm,

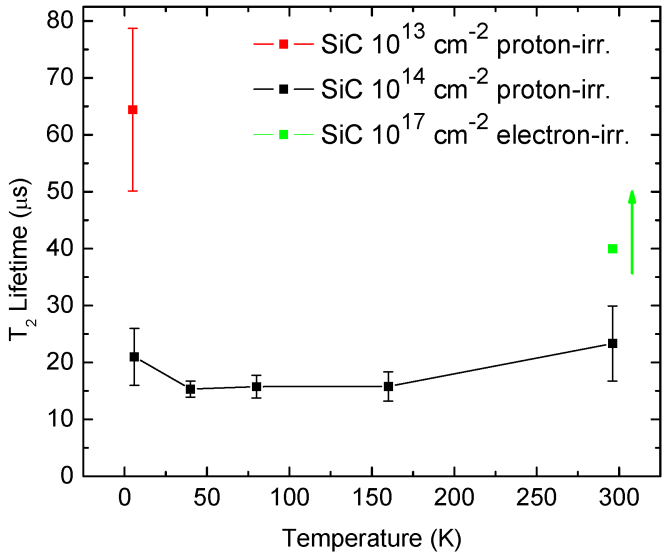

Figure 3.11 T_2 spin lifetime values for all samples studied. Numerical values are found in Table 3.1. Note that we can only establish a lower limit for the lifetime of the 10^{17} cm^{-2} electron-irradiated sample.

but there are extra defects where the protons stop inside the material. These extra defects would not occur as frequently with less irradiation, and it is possible that there is better coherence for this reason in the 10^{13} cm^{-2} sample. However, data from this sample is a lot more noisy than from the other sample, even at low temperatures. In the future we look to reduce the noise when observing the 10^{13} cm^{-2} sample and measure the lifetime at various temperatures.

Regarding the electron-irradiated sample, our collaborator Sam Carter measured the lifetime of a similar sample to be about 80 μs at lower fields [19]. Thus in order to accurately measure the lifetime of this sample, we must find a way to measure the spin echo signal at much longer delay times. We will then test the electron-irradiated sample at various temperatures and various fields to more accurately characterize its spin lifetime.

Bibliography

[1] D. H. McIntyre, *Quantum Mechanics: A Paradigms Approach*, 1st ed. (Addison-Wesley, 2012), pp. 514–526.

[2] P. W. Shor, "Algorithms for quantum computation: Discrete logarithms and factoring," Proc. 35nd Annual Symposium on Foundations of Computer Science pp. 124–134 (1994).

[3] D. Beckman, A. N. Chari, S. Devabhaktuni, and J. Preskill, "Efficient networks for quantum factoring," Physical Review A **54,** 1034 (1996).

[4] M. L. Bellac, "Towards a Quantum Computer?," The Quantum World. Edited by LE BELLAC MICHEL. Published by World Scientific Publishing Co. Pte. Ltd., 2014. ISBN# 9789814522434, pp. 149-165 **1,** 149–165 (2014).

[5] B. E. Kane, "A silicon-based nuclear spin quantum computer," nature **393,** 133–137 (1998).

[6] J. L. O'Brien, S. R. Schofield, M. Y. Simmons, R. G. Clark, A. S. Dzurak, N. J. Curson, B. E. Kane, N. S. McAlpine, M. E. Hawley, and G. W. Brown, "Towards the fabrication of phosphorus qubits for a silicon quantum computer," Physical Review B **64,** 161401 (2001).

[7] J. Benhelm, G. Kirchmair, C. F. Roos, and R. Blatt, "Towards fault-tolerant quantum computing with trapped ions," Nature Physics **4,** 463–466 (2008).

[8] P. Selinger, "Towards a quantum programming language," Mathematical Structures in Computer Science **14,** 527–586 (2004).

[9] S.-S. Li, G.-L. Long, F.-S. Bai, S.-L. Feng, and H.-Z. Zheng, "Quantum computing," Proceedings of the National Academy of Sciences **98,** 11847–11848 (2001).

[10] S. Luryi, J. Xu, and A. Zaslavsky, "Is FaultTolerant Quantum Computation Really Possible?," (2009).

[11] C. Monroe, "Quantum information processing with atoms and photons," Nature **416,** 238–246 (2002).

[12] R. Vrijen, E. Yablonovitch, K. Wang, H. W. Jiang, A. Balandin, V. Roychowdhury, T. Mor, and D. DiVincenzo, "Electron-spin-resonance transistors for quantum computing in silicon-germanium heterostructures," Physical Review A **62,** 012306 (2000).

[13] F. Brennecke, T. Donner, S. Ritter, T. Bourdel, M. Köhl, and T. Esslinger, "Cavity QED with a Bose–Einstein condensate," Nature **450,** 268–271 (2007).

[14] D. Loss and D. P. DiVincenzo, "Quantum computation with quantum dots," Physical Review A **57,** 120 (1998).

[15] S. Prawer and A. Greentree, "Diamond for quantum computing," Science **320,** 1601–1602 (2008).

[16] W. F. Koehl, B. B. Buckley, F. J. Heremans, G. Calusine, and D. D. Awschalom, "Room temperature coherent control of defect spin qubits in silicon carbide," Nature **479,** 84–87 (2011).

[17] J. M. Kikkawa and D. D. Awschalom, "Lateral drag of spin coherence in gallium arsenide," Nature **397,** 139–141 (1999).

[18] N. Bar-Gill, L. M. Pham, A. Jarmola, D. Budker, and R. L. Walsworth, "Solid-state electronic spin coherence time approaching one second," Nature communications **4,** 1743 (2013).

[19] S. G. Carter, Ö. O. Soykal, P. Dev, S. E. Economou, and E. R. Glaser, Naval Research Laboratory (unpublished).

[20] D. J. Christle, A. L. Falk, P. Andrich, P. V. Klimov, J. U. Hassan, N. T. Son, E. Janzén, T. Ohshima, and D. D. Awschalom, "Isolated electron spins in silicon carbide with millisecond coherence times," Nature materials (2014).

[21] R. H. Hashemi, W. G. Bradley, and C. J. Lisanti, *MRI: the basics* (Lippincott Williams & Wilkins, 2012).

[22] N. Mizuochi, S. Yamasaki, H. Takizawa, N. Morishita, T. Ohshima, H. Itoh, and J. Isoya, "Continuous-wave and pulsed EPR study of the negatively charged silicon vacancy with S= 3 2 and C 3 v symmetry in n-type 4 H-SiC," Physical Review B **66,** 235202 (2002).

[23] G. W. Morely, "Spin Echo GWM Stills,", http://commons.wikimedia.org/wiki/File%3ASpin Echo_GWM_stills.jpg, 2015.

[24] M. Widmann, S.-Y. Lee, T. Rendler, N. T. Son, H. Fedder, S. Paik, and L.-P. Yang, "Coherent control of single spins in silicon carbide at room temperature," Nature materials (2014).

[25] F. Bechstedt, P. Käckell, A. Zywietz, K. Karch, B. Adolph, K. Tenelsen, and J. Furthmüller, "Polytypism and properties of silicon carbide," physica status solidi (b) **202,** 35–62 (1997).

[26] J. Peatross and M. Ware, *Physics of Light and Optics* (2015 edition), p. 292, available at optics.byu.edu.

[27] R. B. Whatley, Z. Zhou, and K. L. Melde, "Reconfigurable RF impedance tuner for match control in broadband wireless devices," Antennas and Propagation, IEEE Transactions on **54,** 470–478 (2006).

[28] C. Hoarau, N. Corrao, J.-D. Arnould, P. Ferrari, and P. Xavier, "Complete design and measurement methodology for a tunable RF impedance-matching network," Microwave Theory and Techniques, IEEE Transactions on **56,** 2620–2627 (2008).

[29] D. Hsu and J. L. Skinner, "On the thermal broadening of zero-phonon impurity lines in absorption and fluorescence spectra," The Journal of chemical physics **81,** 1604–1613 (1984).

[30] D. Riedel *et al.*, "Resonant addressing and manipulation of silicon vacancy qubits in silicon carbide," Phys. Rev. Lett. **109,** 226402 (2012).

Index